DOI: 10.65731/ama/2026-0073 *acta mechanica et automatica, vol. 20 no. 3 (2026)*

MULTI-OBJECTIVE NSGA-II OPTIMIZATION WITH ARRHENIUS AND JOHNSON-COOK CONSTITUTIVE MODELING OF DUCTILE CAST IRON AT ELEVATED TEMPERATURE

Mohammed Y. ABDELLAH[*/], Shadi SALEM[**/***], Hasan H. HIJJI[****], Ahmed MALLOULI[**/*****]**

[*]Mechanical Engineering Department, Faculty of Engineering, Qena University, Qena 83521, Egypt
[**]Mechanical Engineering department, College of Engineering, Alasala Colleges, Dammam 31483, Saudi Arabia
[***]Physics Department, Faculty of Science, Al-Balqa Applied University, Al-Salt 19117, Jordan
[****]Mechanical Engineering Department, College of Engineering and Architecture, Umm Al-Qura University, P.O. Box 5555, Makkah 21955, Saudi Arabia
[*****]National Engineering School of Sousse (ENISO), University of Sousse, Sousse 4023, Tunisia

Mohammed.ahmad@alasala.edu.sa, shadi.salem@alasala.edu.sa, hhhijji@uqu.edu.sa, ahmed.melllouli@alasala.edu.sa

received 16 January 2026, revised 27 June 2026, accepted 10 July 2026

Abstract: Temperature and strain rate exert a profound influence on the thermo-mechanical behavior and structural integrity of ductile cast iron operating under elevated-temperature service conditions. In this study, an experimental investigation was conducted over temperatures ranging from 25 to 850 °C and strain rates of 1.8×10^{-4}, 9×10^{-4}, and 4.5×10^{-3} s^{-1}. Tensile testing revealed pronounced thermal softening, with ultimate tensile strength decreasing from 761.5 MPa at room temperature to below 100 MPa at 850 °C, while fracture strain increased to a maximum of 2.2%, indicating enhanced ductility at elevated temperatures. Fracture toughness was evaluated using experimentally validated XFEM simulations, showing a substantial reduction from 54.66 kJ/m² at room temperature to 23.9 kJ/m² at 850 °C. To establish predictive relationships between processing conditions and mechanical performance, Arrhenius-type and Johnson–Cook constitutive models were calibrated and systematically compared. The Johnson–Cook formulation demonstrated significantly superior predictive capability, achieving coefficients of determination of $R^2 = 0.91$ and 0.92 for ultimate and yield strengths, respectively, compared with R^2 values below 0.52 for the Arrhenius model. Building on the validated constitutive framework, a multi-objective optimization strategy based on the Non-dominated Sorting Genetic Algorithm II (NSGA-II) was developed to simultaneously optimize strength, ductility, and fracture toughness. The resulting Pareto fronts quantified the inherent trade-offs among competing mechanical properties and enabled the identification of optimal thermo-mechanical processing windows. The proposed integrated experimental–computational framework provides a validated methodology for constitutive characterization, performance prediction, and materials design optimization of ductile cast iron under severe thermo-mechanical environments. The findings demonstrate the potential of combining constitutive modeling, fracture mechanics, and evolutionary multi-objective optimization to accelerate the development of high-performance engineering alloys.

Key words: ductile cast iron, constitutive modeling, fracture toughness, multi-objective optimization (NSGA-II)

1. INTRODUCTION

Ductile cast iron (also known as nodular cast iron) differs from grey cast iron due to the presence of spheroidal graphite inclusions. These inclusions enhance ductility and significantly improve resistance to impact and fatigue. The rounded shape of the graphite contributes to strong performance and durability at high temperatures, along with good mechanical properties, ease of casting, and low production costs. Thanks to these benefits, ductile cast iron is widely used in engineering applications [1]. In many cases, it competes directly with steel [2]. Structurally, cast iron differs from steel mainly in formation and amount of carbon or graphite particles. The properties of cast iron are heavily influenced by the shape of these particles. In ductile cast iron, the spheroidal graphite controls both how the material solidifies and how it deforms under stress [3]. Another advantage of this alloy is that its desired microstructure can be achieved without heat treatment, simply by adjusting the alloying elements. Compared to steel, key factors include fatigue resistance, production cost, and mechanical strength [4-8].

Amiri Kasvayee [9] studied the deformation behavior of ductile cast iron during tensile testing using digital image correlation. He described the failure process as starting with cracks inside the graphite nodules, followed by separation between the graphite and the surrounding matrix, then the formation and growth of voids around the nodules, and finally the merging of microcracks into larger cracks. In this way, the graphite nodules act as stress concentrators, weakening the matrix. In contrast, Dong et al. [10] observed different deformation patterns during in situ tensile testing.

Ductile cast iron is also used in heavy-duty engine exhaust manifolds, where creep and creep fatigue are major concerns [11]. In these applications, voids tend to form around graphite nodules, creating stress concentration points that lead to creep damage [12, 13]. Torre et al. [14] investigated how section size, holding temperature, and holding time affect mechanical properties during thermo-mechanical treatment, finding that both temperature and time have a strong influence. Angella et al. [15] examined the role of silicon, noting that higher silicon levels speed up the breakdown of chunky graphite [16], which lowers tensile strength but improves oxidation resistance and microstructural stability at high temperatures [17].

More recently, Bendikienė et al. [18] showed that bainitisation temperature affects toughness, hardness, and fatigue resistance.

As temperature increases, hardness decreases, and the fracture surface changes from cleavage to ductile dimple rupture.

Kobayashi and Yamada [19] measured fracture toughness using three-point bending tests, reporting an average initiation toughness (J_1C) of 51.4 kJ/m² and noting that dynamic toughness was lower than static toughness. Artola et al. [20] used a wedge mold design to evaluate tensile, impact, and fracture toughness, showing that mechanical performance and toughness vary depending on the maintenance temperature. Alloying elements also influence toughness: copper and copper–nickel were found to reduce it [21, 22]. Putatunda [23, 24] explored multi-step bainitisation treatments and concluded that fracture toughness is mainly affected by the amount of ferrite and the shape of the graphite, with significant improvements achieved under optimized conditions.

Other methods for analyzing fracture behavior include local fracture models. Techniques like cohesive zone modeling and modified Gurson's potential have been used to simulate crack growth and void formation in ductile cast iron, successfully predicting toughness under various loading conditions [25, 26]. The high-temperature performance of grades such as GGG400SiMo has been studied under both slow and fast strain rates up to 600 °C, showing that creep becomes the main deformation mechanism above roughly 425 °C [27, 28]. More recently, Basurto-Hurtado et al. [29] introduced a method for modeling microstructure geometry using image processing and Bézier curve fitting to represent graphite nodules. This approach links microstructural features to stress distribution through finite element analysis.

Mathematical modeling of high-temperature flow stress plays a critical role in optimizing hot working processes [30, 31]. A range of constitutive equations both phenomenological and physically based have been developed to describe the flow behavior of metallic materials [32]. Among these, the Johnson-Cook model [33] is widely applied across various alloys, including magnesium, aluminum, steels, and titanium [34-36], capturing the influence of strain, strain rate, and temperature [37]. The hyperbolic sine Arrhenius-type model has also demonstrated strong predictive capability for hot deformation behavior [38, 39]. Comparative studies, such as that by Abbasi-Bani et al. [34], indicate that the Arrhenius-type model often yields higher accuracy than Johnson-Cook in modeling flow stress. Furthermore, the high-temperature flow behavior of additively manufactured 316L stainless steel was studied via hot compression tests at 973–1273 K and strain rates of 0.001–0.1 s^{-1}. While Arrhenius-type and Johnson-Cook models were applied, both showed limitations in predicting flow stress and deformation behavior. A feedforward artificial neural network was developed using strain, strain rate, and temperature as inputs, yielding superior accuracy in modeling flow stress across conditions [40].

In addition to traditional plastic deformation modeling, metal behavior goes through an optimization process. For this process, a multi-objective genetic algorithm, guided by ANN-based models, was used to optimize the processing schedule of Ti-49 at.% Ni alloy for improved shape recovery and mechanical properties. Pareto-optimal solutions informed process design, which was experimentally validated [41]. Building on this, a hybrid framework combining NSGA-III and Light GBM is proposed to simultaneously optimize yield strength, ultimate tensile strength, and elongation in Mg alloys. This marks the first successful application of machine learning for multi-objective property optimization in this system, overcoming the limitations of single-target predictions and validating the approach through experimental results [42]. Building on this methodology, ultrasonic rolling process parameters were optimized through a multi-objective framework based on NSGA-II. Predictive models were employed to establish quantitative relationships between process variables and surface characteristics, including residual stress, hardness, and roughness. Experimental validation demonstrated that the optimized parameters led to substantial improvements in fatigue life and surface integrity compared to both untreated and non-optimized conditions [43]. Furthermore, nitrogen-containing gray cast iron is a high-strength, environmentally clean material with promising industrial applications. However, its enhanced properties present challenges in machining, particularly in achieving both efficiency and surface quality. This study investigates the milling behavior of the material, analyzing the influence of cutting parameters on force, temperature, and surface roughness. An integrated optimization approach, combining non-dominated sorting and hierarchical analysis, was employed to identify optimal machining conditions under varying production requirements. The findings provide a practical basis for improving machinability and advancing the application of this material in engineering contexts [44]. Complementarily, recent efforts in multi-objective optimization have advanced both design generation and machining efficiency. A novel genetic algorithm incorporating an offspring selection strategy was formulated as a multi-objective problem, guided by criteria such as space-fillingness, resemblance, diversity preservation, and constraint satisfaction. This approach was benchmarked against conventional selection techniques across simulation-driven and mechanical design scenarios [45]. In parallel, optimization of turning parameters for EN24 steel with tungsten carbide tools was conducted using differential evolution and non-dominated sorting methods, aiming to minimize tool wear and maximize material removal rate under surface roughness and temperature constraints. Comparative analysis confirmed the effectiveness of both strategies in improving performance across their respective domains [46].

The article hypothesizes that ductile cast iron exhibits temperature and strain rate dependent mechanical behavior and fracture behavior, and that this can be reliably described by constitutive modeling (Arrhenius and Johnson-Cook-like frameworks). In this way, it is possible to capture the deterioration of strength and toughness at high temperatures and higher strain rates. This study presents a comprehensive experimental investigation of ductile cast iron covering a wide range of temperatures between 25 °C and 850 °C and strain rates of 1, 5, and 25 mm/min. Under these controlled conditions, important mechanical properties are investigated simultaneously, including tensile strength (σ_u), yield strength (σ_Y), elongation at break (εf), and fracture toughness (J_{IC}). This fills a notable gap in the existing literature, where such simultaneous assessments are rarely reported. Furthermore, this paper presents a comparative analysis of two constitutive modeling approaches: the classical Arrhenius regression and a Johnson-Cook inspired formulation. This comparison illustrates the predictive capabilities and inherent limitations of each model in capturing the thermomechanical behavior of the material. To improve the applicability in design, the study integrates the strain-at-failure regression with multi-objective optimization through the non-dominated genetic sorting algorithm II (NSGA-II), allowing the identification of optimal performance ranges for ductile cast iron components under different operating conditions.

This study investigates the mechanical response of ductile cast iron under varied thermal and loading conditions. (1) It experimentally characterizes tensile strength (σ_u), yield strength (σ_Y), fracture strain (ε_f), and fracture toughness (J_{IC}) across temperature and strain rate ranges, yielding a consistent dataset for analysis and modeling. (2) Constitutive models for σ_u and σ_Y are developed using Arrhenius-type and Johnson-Cook-like formulations to assess predictive accuracy. (3) Regression models for ε_f and J_{IC} quantify ductility and toughness. (4) Model performance is evaluated using R^2 and RMSE, and the results are integrated into a multi-objective Pareto optimization framework to explore trade-offs among strength, ductility, and toughness, thereby identifying optimal design domains for engineering applications.

While previous studies by the authors [47] focused on fracture toughness prediction via XFEM simulations without constitutive modeling, and other investigations [48] characterized basic tensile properties at room temperature, the present work provides the first integrated framework combining (i) experimental characterization across three strain rates and four temperatures, (ii) comparative constitutive modeling using Arrhenius and Johnson-Cook formulations, and (iii) NSGA-II Pareto optimization to identify optimal processing conditions. This integration represents a significant advance beyond prior isolated analyses.

2. MATERIAL CHARACTERIZATION

The ductile cast iron used in this study was a commercial grade produced specifically for this research and sourced from the Egyptian Iron and Steel Company (Hadisolb), located in Helwan, Egypt. Its chemical composition is detailed in Table 1 [48]. As a commercial product manufactured for research purposes, it was not supplied with a specific standard grade designation (e.g., EN-GJS or ASTM A536 class). The chemical composition (Table 1) is consistent with a high-strength, low-ductility grade of ductile cast iron, with a predominantly pearlitic matrix. The low room-temperature elongation (0.59%) and high tensile strength (761.5 MPa) support this classification. However, it is acknowledged that no metallographic analysis (optical microscopy, phase fraction) was performed to confirm the matrix microstructure, and this remains a limitation of the present study.

Tab. 1. Chemical composition of the tested cast iron (wt%) adapted from Ref. [48]

Element	C%	Si%	Mn%	P%	S%	Balanced Fe
Contents (mg)	3.0–3.6	2.0–2.5	0.6	0.04 max	0.04	

The mechanical properties of the material were evaluated through tensile testing conducted at room temperature (25 °C) using a crosshead speed of 1 mm/min. In accordance with ASTM E8 [49], the ultimate tensile strength, yield strength, and elongation were determined to be 761.5 MPa, 316.8 MPa, and 0.59%, respectively. The chemical composition presented in Table 1 is adopted from our previous characterization study [49]. However, the tensile data at elevated temperatures (750 °C and 850 °C) reported in the present study have been updated to include the corresponding Young's modulus values, as presented in Table 2.

Tab. 2. Average mechanical properties of ductile cast iron (Young's modulus values are reported with an estimated measurement uncertainty of ±10% due to the use of crosshead displacement for strain measurement)

Property	**Strain rate (s^{-1})**	**25 °C**	**450 °C**	**750 °C**	**850 °C**
Young’s modulus E (GPa)	1.8×10^{-4}	240	215	158	105
	9×10^{-4}	235	174	130	100
	4.5×10^{-3}	171	177	125	37
Ultimate strength σu (MPa)	1.8×10^{-4}	761.5	684.1	231.6	78.8
	9×10^{-4}	741.3	578.4	55.7	92.2
	4.5×10^{-3}	584	351	132.7	78.7
Yield stress σy (MPa)	1.8×10^{-4}	316.8	219.26	104.8	32.4
	9×10^{-4}	276.24	221.6	48.4	40.5
	4.5×10^{-3}	255.8	222.12	88.47	30.4
Fracture strain εf (%)	1.8×10^{-4}	0.56	0.62	1	0.9
	9×10^{-4}	0.54	0.91	1.61	1.71
	4.5×10^{-3}	0.577	0.47	0.773	2.20

2.1. Experimental Work

The tensile specimens of cast iron were machined into circular dog-bone shapes with a diameter of 6 mm and threaded ends, as illustrated in Figure 1. The thermomechanical treatment (T.M.T.) parameters included the exposure temperature and the extent of deformation. Tensile tests were conducted directly at the target elevated temperatures (450°C, 750°C, 850°C) after a 20-minute soaking period. No cooling or post-treatment was applied before testing. The term "thermomechanical treatment" herein refers to the simultaneous application of thermal and mechanical loading during testing, not a separate pre-treatment process.

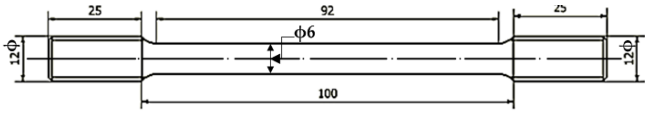

Fig. 1. Standard circular dog bone tensile specimen for thermomechanical treatment (dim. mm)

Specimens were subjected to controlled deformation levels corresponding to 0%, 25%, 50%, 75%, and 100% of the expected fracture displacement (determined from preliminary tests). For example, for a specimen with an expected fracture displacement of approximately 1 mm (corresponding to 0.59% strain over the 170 mm length), 25% deformation corresponds to 0.25 mm displacement, 50% to 0.5 mm, 75% to 0.75 mm, and 100% to fracture. These deformation levels were measured using a dial gauge attached to the moving crosshead.

The dial gauge used to measure strain had a resolution of 0.01 mm and an accuracy of ±0.02 mm, and it was attached to the crosshead. While an elevated-temperature extensometer would provide higher precision, the dial gauge method is considered adequate for the low elongation values (0.54–2.20%) reported herein. Crosshead displacement measurements were recorded simultaneously and showed consistent trends.

All tests were conducted in accordance with ASTM E8 [49]. The experiments were performed at three distinct strain rates: 1.8×10^{-4} s^{-1}, 9×10^{-4} s^{-1}, and 4.5×10^{-3} s^{-1}, corresponding to crosshead speeds of 1, 5, and 25 mm/min, respectively. Although ASTM E8 [1] is primarily intended for room-temperature testing, it was applied with additional temperature control measures (thermocouple monitoring, 20-minute soaking) to ensure reliable elevated-temperature results. The authors acknowledge that ASTM E21 is the dedicated standard for elevated-temperature tension testing and recommend its use in future work.

Temperature homogeneity was verified using three K-type thermocouples positioned at the specimen ends and midpoint, showing ≤ ±3°C variation across the 50 mm gauge length. A 20-minute soaking period was selected based on preliminary thermal equilibrium tests, which indicated stabilization within 12–15 minutes for all target temperatures.

For each combination of temperature (25°C, 450°C, 750°C, 850°C) and strain rate (1.8×10^{-4}, 9×10^{-4}, 4.5×10^{-3} s^{-1}), three tensile specimens were tested (N = 3). The reported values in Table 2 represent the arithmetic mean of these three measurements. Standard deviations for ultimate strength were within ±5% of mean values.

2.2. Methodology

Fracture toughness (JIC) values were obtained from XFEM simulations using the extended finite element method implemented in Abaqus. All values (SR1, SR2, and SR3) were extracted from XFEM simulations. The XFEM model was validated at room temperature (25°C) for SR1 condition (1.8×10^{-4} s^{-1}) against compact tension (CT) test results from Kobayashi and Yamada [19], showing good agreement (XFEM: 54.6 kJ/m², Experimental: 51.4 kJ/m²). However, no experimental validation exists for elevated temperatures (450°C, 750°C, and 850°C) or for SR2 and SR3 conditions.

3. Non-dominated Sorting Genetic Algorithm II (NSGA-II)

The NSGA-II algorithm, as implemented in the provided Python code (pareto.py), optimizes a multi-objective problem for ductile cast iron properties. The code uses the pymoo library to apply NSGA-II on a custom problem class, where the decision variables are temperature TC (in °C, bounded (25, 850)) and log-strain rate proxy (log speed, bounded (-0.3, 2), corresponding to crosshead speed (v) in mm/min ≈ (1, 5, 25)). The objectives are to maximize ultimate strength σ_u (MPa), fracture toughness J_{IC}, and fracture strain ε_f (%). Since NSGA-II is framed as a minimization algorithm, the objectives are negated.

Now go through derivation of the model, let $x \in$ X denote the decision vector, where $x = [T_C, \log \nu]$, $K_k = T_C + 273.15$, and $\nu = 10^{\log(\nu)}$ (strain -rate proxy in mm/min). The objective vector to maximize is as follows[50]:

$$f(x) = \left[\sigma_u(x), J_{IC}(x), \varepsilon_f(x)\right] \tag{1}$$

For NSGA-II minimization:

$$\min_{x \in \mathrm{X}} f(x) = \left[-\sigma_u(x), -J_{IC}(x), -\varepsilon_f(x)\right] \tag{2}$$

with constrains X: $25 \ \le \mathrm{T}_C \le 850, -0.3 \le \log \nu \le 2$

3.1. Pareto model

For two feasible decisions $a, b \,\epsilon\, \mathrm{X}$ with objective vector $\check{f}(a)\ and\ \check{f}(a)$ (to be minimized), a a pareto dominates b (denoted $a \prec b$) if:

$$\check{f}(a) \le \check{f}(a) \qquad \forall_i \,\epsilon\, \{1,2,3\} \tag{3}$$

and

$$\exists_i:\ \check{f}(a) \le \check{f}(a) \tag{4}$$

A decision a is Pareto-optimal if no b exists such that $b \prec a$. The Pareto front is the image of all Pareto optimal decision in objective space.

3.2. NSGA-II Mechanics

NSGA-II approximates the Pareto front using non-dominated sorting (assigning front ranks F1, F2, where F1 is the first non-dominated front) and crowding distance (a diversity metric: per-objective, range-normalized sum of nearest-neighbor gaps in objective space). Selection favors lower ranks and higher crowding distances. The algorithm runs for a specified number of generations (e.g., 80 in the present analysis) with population size (e.g., 80).

Population size (80) was selected as approximately 10× the number of decision variables (n_var = 2) following Deb et al. [50] recommendations. The convergence behavior of the NSGA-II algorithm was evaluated using the hypervolume (HV) metric. As presented in Supplementary Figure S1, the hypervolume increased rapidly during the early generations and stabilized after approximately Generation 14, indicating successful convergence toward a stable Pareto-optimal front. Subsequent generations produced only marginal improvements, confirming that the selected population size and number of generations (80) were sufficient for obtaining converged optimization results. The generational distance between successive Pareto fronts fell below 10^{-3} after generation 72.

3.3. Constitutive/Response Models

– **Fracture Strain Model**

The fracture strain (ε_f, %) was correlated with temperature and crosshead speed using a linear regression model [51]:

$$\varepsilon_f(T_K,\nu)=\rho_0\left(\frac{1}{T_K}\right)+\rho_1\ln(\nu)+\rho_2 \quad (5)$$

where ε_f is the fracture strain (%), T_K is the absolute temperature (K), ν is the crosshead speed (mm/min), and ρ_0, ρ_1, and ρ_2 are regression coefficients determined by the least-squares fitting method.

The fracture strain in fractional form is expressed as:

$$\varepsilon_{\mathrm{Fra}}=\frac{\varepsilon_f}{100}$$

– **Strength Prediction Model**

The ultimate tensile strength (σ_u) and yield strength (σ_y) were described using a modified Johnson–Cook constitutive model [33]:

$$\sigma(T_K,\nu,\varepsilon_{\mathrm{Fra}})=\left[A+B\left(\max(\varepsilon_{\mathrm{Fra}},10^{-6})\right)^n\right]\left(1+C\ln\left(\frac{\nu}{\nu_0}\right)\right)(1-T^*)^m \quad (6)$$

where

$$T^*=\max\left[0,\min\left(1,\ \frac{T_K-298}{1123-298}\right)\right]$$

and $\varepsilon_{\mathrm{Fra}}$ is the fracture strain in fractional form, ν is the crosshead speed (mm/min), and $\nu_0=1.0$ mm/min is the reference crosshead speed. The material constants A, B, C, n, and m were identified through parameter optimization by minimizing the mean squared error (MSE) between experimental and predicted values which listed in Table 3.

Tab. 3. The calibrated Johnson–Cook and Arrhenius model parameters

	Parameter	**σ_u(MPa)**	**σ_y(MPa)**
Johnson–Cook	A(MPa)	723.78	291.76
	B(MPa)	558.70	23.98
	n	0.249	0.450
	C	-0.102	-0.054
	m	0.635	0.500
Arrhenius	a	4.5003	3.7306
	b (K)	716.92	636.43
	c	-0.1158	-0.0337

Note: Reference crosshead speed v_0 = 1.0 mm/min, room temperature T_{room} = 298 K, melting temperature T_{melt} = 1123 K

It should be noted that the temperature normalization parameter T_{melt} = 1123 K was adopted as an effective calibration parameter within the Johnson–Cook constitutive model. Although the actual melting temperature of ductile cast iron is higher (approximately 1423 K), the use of the physical melting temperature during model calibration resulted in a noticeable reduction in predictive accuracy. Consequently, the selected value was retained to provide improved representation of the experimentally observed thermal softening behavior over the investigated temperature range (25–850°C). Accordingly, Tmelt should be regarded as a phenomenological fitting parameter rather than a physical melting temperature, and the applicability of the model is restricted to the experimentally validated temperature range considered in this study.

– **Fracture Toughness Model**

The fracture toughness (J_{IC}) was correlated with temperature and crosshead speed using a linear regression model [51]:

$$J_{IC}(T_K,\nu)=a_JT_K+b_J\ln(\nu)+c_J \quad (7)$$

where J_{IC} is the fracture toughness ($\mathrm{kJ/m^2}$), T_K is the absolute temperature (K), ν is the crosshead speed (mm/min), and a_J, b_J, and c_J are regression coefficients obtained using the least-squares fitting procedure.

4. RESULTS AND DISCUSSION

4.1. Effect of Temperature

Figures 2a, 2c, and 2e illustrate the evolution of ultimate tensile strength (σu) as a function of fracture strain (εf) for ductile cast iron subjected to tensile testing at strain rates of 1.8 × 10^{-4} s^{-1} (SR1), 9 × 10^{-4} s^{-1} (SR2), and 4.5 × 10^{-3} s^{-1} (SR3), respectively. The data clearly indicate that increasing temperature leads to a reduction in both tensile strength and elastic modulus, while ductility improves. This enhancement in ductility is evident from the increased percentage elongation at fracture, also referred to as percentage strain. Temperature is a critical factor influencing the mechanical behavior of the material. As strength and stiffness decline with rising temperature, the material exhibits greater deformability, as shown by the elongation metrics. Assuming that higher strain rates positively influence the deformation characteristics and ductility of cast iron, the average percentage strain at 850 °C reached 2.20% at a strain rate of 4.5 × 10^{-3} s^{-1}, as presented in Table 2 and Figures 2b, 2d, and 2f. However, when the material is exposed to elevated temperatures within the range of 673–773 K, embrittlement is observed [52, 53]. This embrittlement is attributed to the segregation of elements such as phosphorus and sulfur at the grain boundaries.

DOI: 10.65731/ama/2026-0073

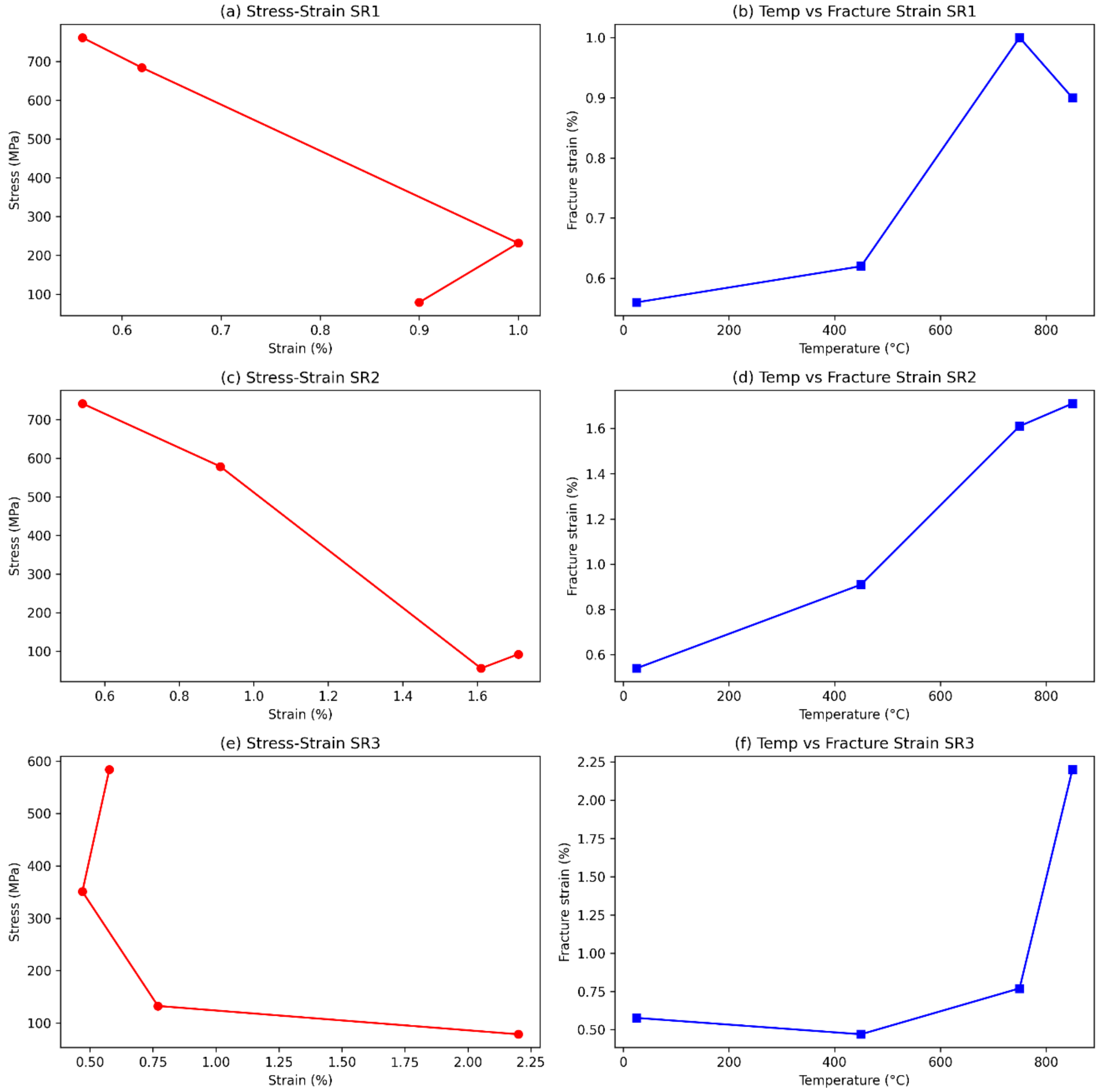

Fig. 2. Evolution of ultimate tensile strength (σu) as a function of fracture strain (εf) at different temperatures for (a) SR1, (c) SR2, and (e) SR3. Temperature dependence of fracture strain at (b) SR1, (d) SR2, and (f) SR3

The non-monotonic mechanical response at 850°C, particularly the yield strength values of 32.4 MPa (SR1), 40.5 MPa (SR2), and 30.4 MPa (SR3) as reported in Table 2, may be attributed to dynamic strain aging (DSA) and partial dissolution of phosphorus-rich grain boundary segregates, as suggested in the literature [53, 54]. At this temperature, which approaches the solidus of low-melting-point eutectics in ductile cast iron, localized microstructural instability—including potential incipient melting of phosphide eutectics—could temporarily impede dislocation motion, leading to anomalous strength recovery. However, we note that direct microstructural evidence (e.g., TEM, EDS) was not obtained in the present study. The proposed mechanisms are therefore hypotheses based on previously reported behavior in similar cast iron grades [53, 54]. Future work should include detailed microstructural characterization to confirm these mechanisms [52, 53].

It can be seen that the strain hardening coefficient generally increases with temperature. At lower strain rates, this coefficient reflects the degree of hardening of the material as deformation progresses. With increasing temperature, ductility improves because the imposed strain is more uniformly distributed, reducing the tendency for local strain concentration [54]. At higher strain rates, however, the strain hardening coefficient exhibits a different behavior: the rapid application of strain produces sudden elongation of grains and stretching of atomic bonds, which in turn lowers both the strength and the strain hardening coefficient. Such effects highlight the importance of understanding the response of ductile cast iron under different loading rates in order to design materials that retain adequate performance under service conditions [55]. Both stiffness stress and yield stress were found to decrease with increasing temperature across all strain rates. The highest average fracture strains reached 1.0% and 1.5% at 750 °C for strain rates of $1.8 \times 10^{-4}\ s^{-1}$ and $9 \times 10^{-4}\ s^{-1}$, respectively, and 1.7% and 2.2% at 850 °C for strain rates of $9 \times 10^{-4}\ s^{-1}$ and $4.5 \times 10^{-3}\ s^{-1}$, respectively (see Table 2). These results confirm that strain rate exerts a significant influence on the flow behavior of ductile cast iron. The relationship between average ultimate strength and strain rate using a power-law fit is presented in Figure 3. It can be seen that the ultimate strength decreases as the strain rate increases from $1.8 \times 10^{-4}\ s^{-1}$ to $4.5 \times 10^{-3}\ s^{-1}$. This trend is accurately captured by the fitted power-law fit (red dashed line), which follows the relationship: $\sigma = 141.67 \times \dot{\varepsilon}^{-0.1325}$.

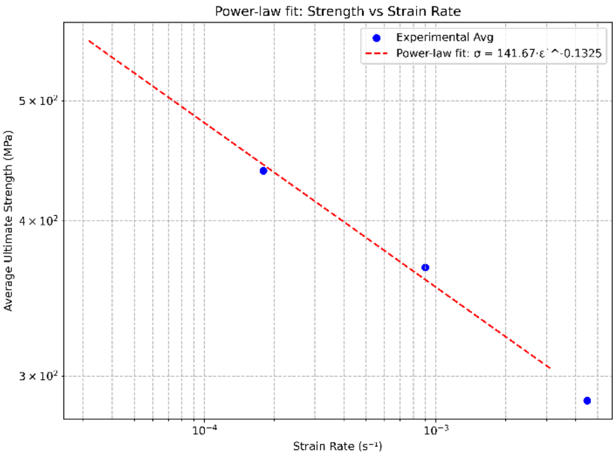

Fig. 3. Average ultimate strength and strain rate relation using Power-law fit

Fractographic analysis of the fracture surfaces was conducted using a scanning electron microscope (SEM) (JEOL JSM-IT500, Tokyo, Japan), as illustrated in Figure 4. In the brittle fracture mode depicted in Figure 4a, the surface exhibited a rough morphology, indicative of damage propagation through voids initiated at graphite nodules. This behavior is attributed to weak interfacial bonding, which facilitated the presence of numerous graphite nodules on the fracture surface [53].

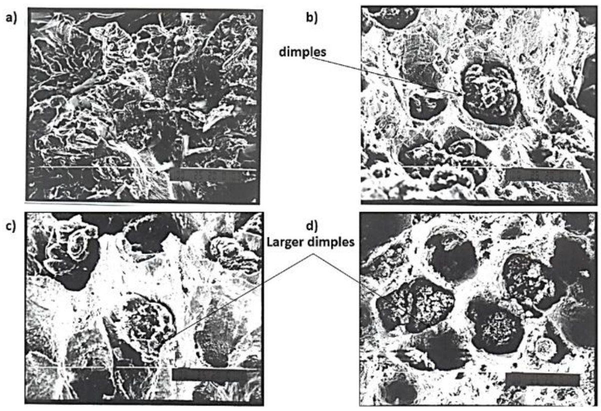

Fig. 4. SEM analysis of ductile cast iron failure under tension [47]

Following the coalescence of linearly aligned voids, the formation of oval-shaped shear dimples was observed, resulting in a smoother and more planar fracture surface (Figure 4b). The quantity and dimensions of these dimples increased progressively with elevated testing temperatures (Figures 4c and 4d). This trend reflects the influence of enhanced plastic deformation, increased energy dissipation, microstructural evolution, and temperature-dependent material responses on the ductile fracture process. The presence and morphology of dimples serve as microstructural indicators of the material's deformation behavior under applied stress [56, 57].

Figure 4 presents representative SEM images of fracture surface morphologies in ductile cast iron specimens subjected to varying test conditions:

– A relatively coarse surface characterized by interconnected voids and tearing ridges, typical of ductile fracture.
– A magnified region displaying dimples, which are hallmark features of microvoid nucleation, growth, and coalescence. These dimples are associated with localized decohesion around graphite nodules and non-metallic inclusions.
– A fracture surface where graphite nodules are distinctly visible, surrounded by a plastically deformed matrix. The nucleation of dimples around these nodules indicates progressive void growth and linkage.
– A surface exhibiting a higher density of enlarged dimples, suggestive of substantial plastic deformation prior to final fracture. The increase in dimple size and density at elevated temperatures or strains enhances ductility but may compromise fracture strength.

These observations align with the established ductile fracture mechanism in nodular cast irons, which involves crack initiation within or at the interface of graphite nodules, void growth around nodules due to localized stress concentration, and coalescence of voids into larger dimples, resulting in a characteristic ductile morphology. At elevated deformation temperatures or under conditions promoting increased ductility, the dimples become more pronounced, larger, and deeper, indicating the matrix's capacity to accommodate greater plastic strain prior to failure. In contrast, smaller or shallower dimples reflect limited plastic deformation and earlier onset of fracture.

Figure 5 illustrates the combined effects of temperature, strain, and strain rate on the mechanical response of ductile cast iron. As shown in Figure 5a, stress decreases markedly with increasing temperature across all strain rates, while higher strain rates sustain relatively higher stress levels, reflecting the material's strain rate sensitivity. Figure 5b demonstrates that fracture toughness similarly declines with increasing temperature, particularly above 600 °C, with higher strain rates mitigating toughness loss to some extent. The surface representation in Figure 5c reinforces these trends, highlighting that stress is strongly dependent on temperature and strain rate, whereas the influence of strain remains secondary. Overall, these results indicate that ductile cast iron undergoes significant thermal softening and toughness reduction at elevated temperatures, although higher strain rates provide a stabilizing effect against degradation.

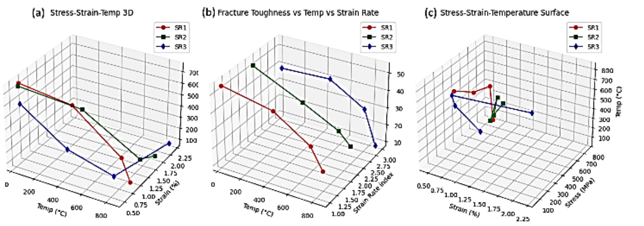

Fig. 5. 3D representation of ductile cast iron: (a) stress–strain–temperature, (b) fracture toughness vs. temperature/strain rate, (c) stress–strain–temperature surface map

Figure 6 further illustrates the thermo-mechanical behavior of ductile cast iron through von Mises stress distribution and safety factor evaluation. As shown in Figure 6a, the von Mises stress reaches values close to 700 MPa at low temperatures and higher strain rates but decreases significantly with increasing temperature, confirming the strong influence of thermal softening. Figure 6b presents the corresponding safety factor analysis, where the safety margin decreases with reduced ultimate stress, dropping below 0.5 at elevated temperatures. These results emphasize the critical reduction in both strength and reliability of ductile cast iron when exposed to high-temperature conditions, despite the stabilizing influence of strain rate.

DOI: 10.65731/ama/2026-0073

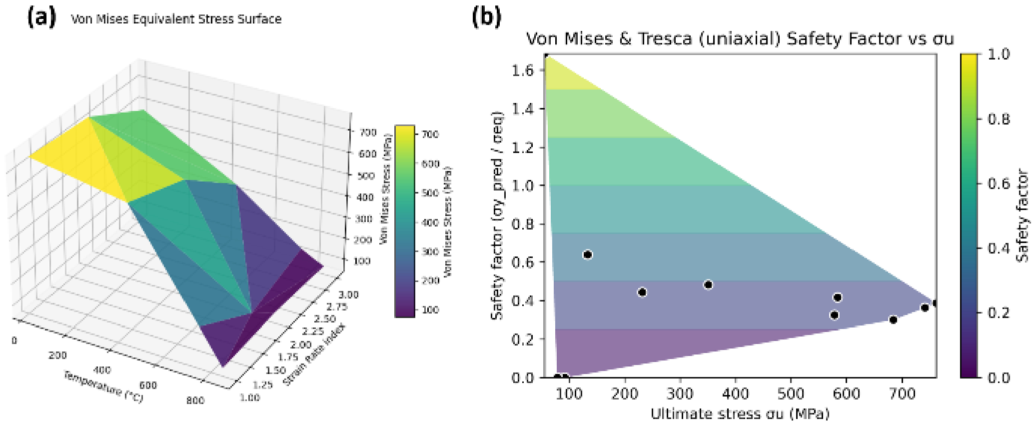

Fig. 6. Thermomechanical response of ductile cast iron: (a) Von Mises stress vs. temperature/strain rate, and (b) safety factor vs. ultimate stress at elevated temperatures

Fracture toughness (J_{IC}) values for ductile cast iron were obtained from XFEM simulations using the Young's modulus reported in Table 2. Table 4 presents the J_{IC} values extracted from these simulations. The XFEM model was validated at room temperature (25°C) for SR1 condition (1.8×10^{-4} s^{-1}) against compact tension test results from Kobayashi and Yamada [19], showing good agreement (XFEM: 54.6 kJ/m², Experimental: 51.4 kJ/m², error: 6.3%). At a strain rate of 1.8×10^{-4} s^{-1} (SR1), J_{IC} decreased from 54.66 kJ/m² at 25°C to 23.9 kJ/m² at 850°C. At a strain rate of 9×10^{-4} s^{-1} (SR2), J_{IC} values ranged from 52.9 kJ/m² at 25°C to 22.7 kJ/m² at 850°C. At the highest strain rate examined (4.5×10^{-3} s^{-1}, SR3), J_{IC} values ranged from 38.8 kJ/m² at 25°C to 8.4 kJ/m² at 850°C. These findings demonstrate a clear inverse relationship between J_{IC} and both temperature and strain rate. The comprehensive fracture toughness dataset is listed in Table 4.

Tab. 4. Fracture toughness JIC (kJ/m²) for SR1 (1.8×10^{-4} s^{-1}) and SR2 (9×10^{-4} s^{-1}), SR3 (4.5×10^{-3} s^{-1}) obtained from XFEM simulations validated against compact tension test [19]

Temperature	Kobayashi and Yamada [19]	$1.8\times10^{-4}\,s^{-1}$	$9\times10^{-4}\,s^{-1}$	$4.5\times10^{-3}\,s^{-1}$
25 °C	51.4	54.66	52.9	38.8
450 °C	N/A	48.9	39.8	40
750 °C	N/A	35.6	29.6	28
850 °C	N/A	23.9	22.7	8.4

It should be noted that the J_{IC} values in Table 4 exhibit non-monotonic trends at intermediate temperatures (e.g., SR3: 38.8 kJ/m² at 25°C, 40.0 kJ/m² at 450°C). This observation correlates with an anomalous Young's modulus value for SR3, where the modulus at 450°C (177 GPa) is slightly larger than at 25°C (171 GPa), suggesting that both anomalies may originate from experimental variability in the elastic regime measurements. This may also be attributed to dynamic strain aging (DSA) effects at intermediate temperatures, which can temporarily enhance fracture resistance through dislocation-solute interactions, consistent with embrittlement behavior reported in the 673–773 K range [52–54]. Similar non-monotonous temperature dependence of mechanical properties has been documented in austempered ductile cast iron, attributed to stress-induced phase transformation of retained austenite [20]. Additionally, studies on solid solution strengthened ferritic ductile cast iron have shown that toughness and strength exhibit abrupt changes at critical strain rates depending on temperature [18]. However, as these values are XFEM-derived and not experimentally validated at elevated temperatures, the combination of high strain rate and intermediate temperature may produce numerical artifacts. The general trend across all other conditions shows a clear monotonic decrease in J_{IC} with increasing temperature, and the 450°C values should be interpreted with caution. Future experimental work is needed to validate these predictions.

4.2. Arrhenius-Model

The predictions obtained from the extended Arrhenius–Johnson–Cook (AJC) model exhibit considerable divergence from the experimental observations. In the case of ultimate tensile strength (σ_u) as a function of temperature (Figure 7a), the model forecasts a consistent decline in strength with increasing temperature across various strain rates. However, the experimental data points (red markers) display pronounced dispersion, particularly at elevated temperatures, indicating substantial deviation from the predicted trend. This discrepancy is quantitatively supported by a low coefficient of determination ($R^2 = 0.48$) and a high root mean square error (RMSE) of 197.5 MPa, suggesting that the model accounts for less than half of the observed variance. A similar pattern is observed for yield stress (σ_Y) versus temperature (Figure 7b), where the model predicts a downward trend, yet the experimental data (green squares) remain widely scattered. The limited predictive capability is further evidenced by $R^2 = 0.51$ and RMSE = 71.4 MPa. Regarding strain-rate dependence (Figures 7c and 7d), the model yields nearly flat curves for both σ_u and σ_Y, with only marginal increases, implying minimal sensitivity to strain rate. Nonetheless, the experimental results again exhibit significant variability. Due to the limited number of data points per temperature (typically two or three), statistical fitting is unreliable, and R^2 values are not reported.

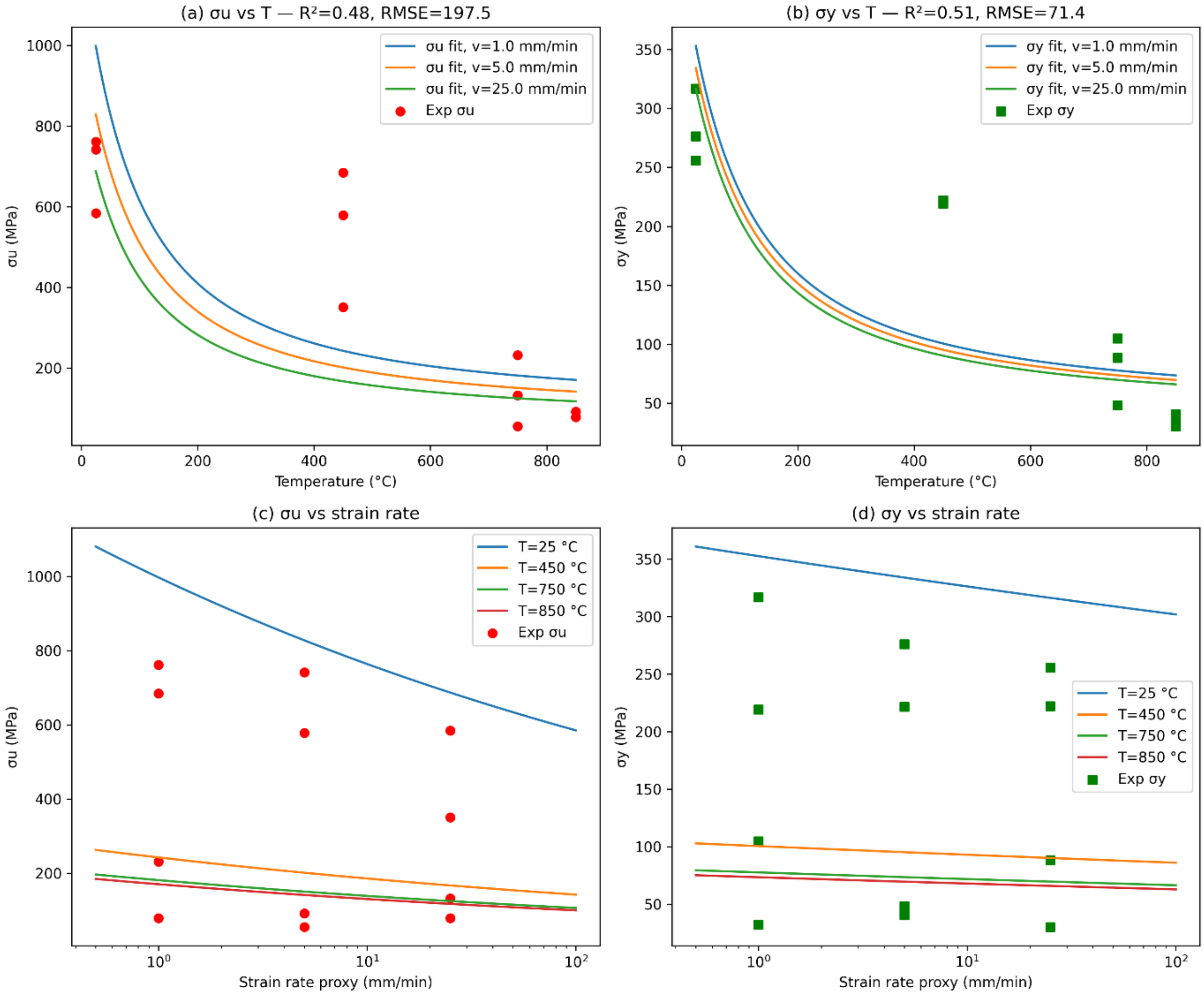

Fig. 7. Arrhenius fits for ductile cast iron: (a) σ_n vs. temperature, (b) σ_Y vs. temperature, (c) σ_n vs. strain rate, (d) σ_Y vs. strain rate

The inadequate performance of the model can be attributed to both its inherent limitations and the characteristics of the dataset. Arrhenius-type formulations presuppose exponential dependence on temperature and logarithmic dependence on strain rate, which are insufficient to represent complex thermomechanical phenomena such as phase transformations, dynamic recovery, creep, and recrystallization, particularly at elevated temperatures. In cast iron, where temperature-dependent mechanisms such as void nucleation and fracture progression are prominent, these simplifications become especially problematic. Additionally, the dataset suffers from sparsity and noise, particularly in the strain-rate series, which undermines the reliability of regression analysis.

These findings are consistent with prior studies. For ductile cast iron (GJS-450), constitutive models based on the Voce formulation, augmented with strain-rate sensitivity and damage mechanics, have demonstrated significantly improved agreement with experimental data [58]. Likewise, investigations involving magnesium alloys have shown that data-driven approaches, including neural network-based models, markedly outperform traditional Arrhenius-type equations in capturing complex thermomechanical behavior [59].

The Arrhenius model is presented here primarily as a baseline comparison. Its low predictive accuracy (R^2 = 0.48 for σ_u, R^2 = 0.51 for σ_y) confirms that the underlying assumptions—exponential temperature dependence and logarithmic strain rate sensitivity—are insufficient for ductile cast iron under these conditions. This justifies the adoption of the more flexible Johnson-Cook formulation, which achieves substantially higher accuracy as shown in Table 5.

Tab. 5. Comparative predictive accuracy of constitutive models

Model	Target	R²	RMSE (MPa)
Arrhenius	σu	0.48	197.5
Arrhenius	σy	0.51	71.4
Johnson-Cook	σu	0.91	83.7
Johnson-Cook	σy	0.92	29.7

The residual plots shown in Figure 8 offer additional evidence of the predictive shortcomings inherent in the Arrhenius-based model. In subplot (Figure 8a), the residuals corresponding to ultimate tensile strength (σ_u) reveal substantial scatter, with deviations ranging from approximately −300 MPa to +500 MPa. The pronounced asymmetry and magnitude of these residuals indicate that the model tends to systematically underestimate the strength under certain conditions and overestimate it under others, particularly at intermediate temperature and strain-rate regimes. Subplot (Figure 8b) presents the residuals for yield stress (σ_Y), which similarly exhibit wide variability, spanning from roughly −250 MPa to +320 MPa. The alternating signs of the residuals suggest that the model fails to consistently capture the underlying mechanical response, reflecting both systematic bias and high variance.

DOI: 10.65731/ama/2026-0073

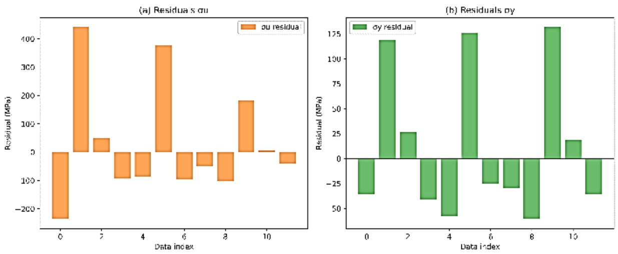

Fig. 8. Residuals of Arrhenius fits: (a) σ_n, (b) σ_Y, showing large deviations that highlight poor predictive accuracy at varying temperatures and strain rates

4.3. Constitutive Modeling Using the Johnson-Cook Framework

To quantify the coupled effects of temperature and strain rate on the mechanical behavior of the investigated ductile cast iron, the experimental ultimate tensile strength (σ_u) and yield strength (σ_Y) data were fitted using the Johnson–Cook (JC) constitutive model. Figure 9 compares the experimental measurements with the calibrated JC model predictions over the investigated thermo-mechanical conditions.

As illustrated in Figures 9a and 9b, both σ_u and σ_Y decrease markedly with increasing temperature from 25 °C to 850 °C, confirming the pronounced thermal softening behavior observed experimentally. The calibrated JC model accurately reproduces this nonlinear reduction in strength, yielding coefficients of determination (R^2) of 0.91 and 0.92 for ultimate tensile strength and yield strength, respectively. The corresponding root mean square errors (RMSEs) were 83.7 MPa for σ_u and 29.7 MPa for σ_Y.

The temperature normalization parameter T_{melt} = 1123 K was adopted as an effective calibration parameter within the phenomenological Johnson–Cook constitutive framework. Although the actual melting temperature of ductile cast iron is higher (approximately 1423 K), using the physical melting temperature during calibration resulted in a reduction in predictive accuracy, with R^2 decreasing from 0.91 to 0.865 for ultimate stress and from 0.92 to 0.870 for yield stress. Consequently, T_{melt} = 1123 K was retained to provide improved agreement with the experimental data over the investigated temperature range (25–850°C). Accordingly, this parameter should be interpreted as a temperature-normalization constant rather than the actual melting temperature of the material, and the model applicability is restricted to the experimentally validated range considered in this study.

Figures 9c and 9d show the variation of strength with strain rate on a logarithmic scale at four isothermal conditions (25 °C, 450 °C, 750 °C, and 850 °C). The JC model successfully captures the strain-rate sensitivity of the material across the investigated testing conditions. Moreover, the model reproduces the convergence of strength values at elevated temperatures (750 °C and 850 °C), where thermal softening becomes the dominant deformation mechanism and diminishes the influence of strain-rate hardening.

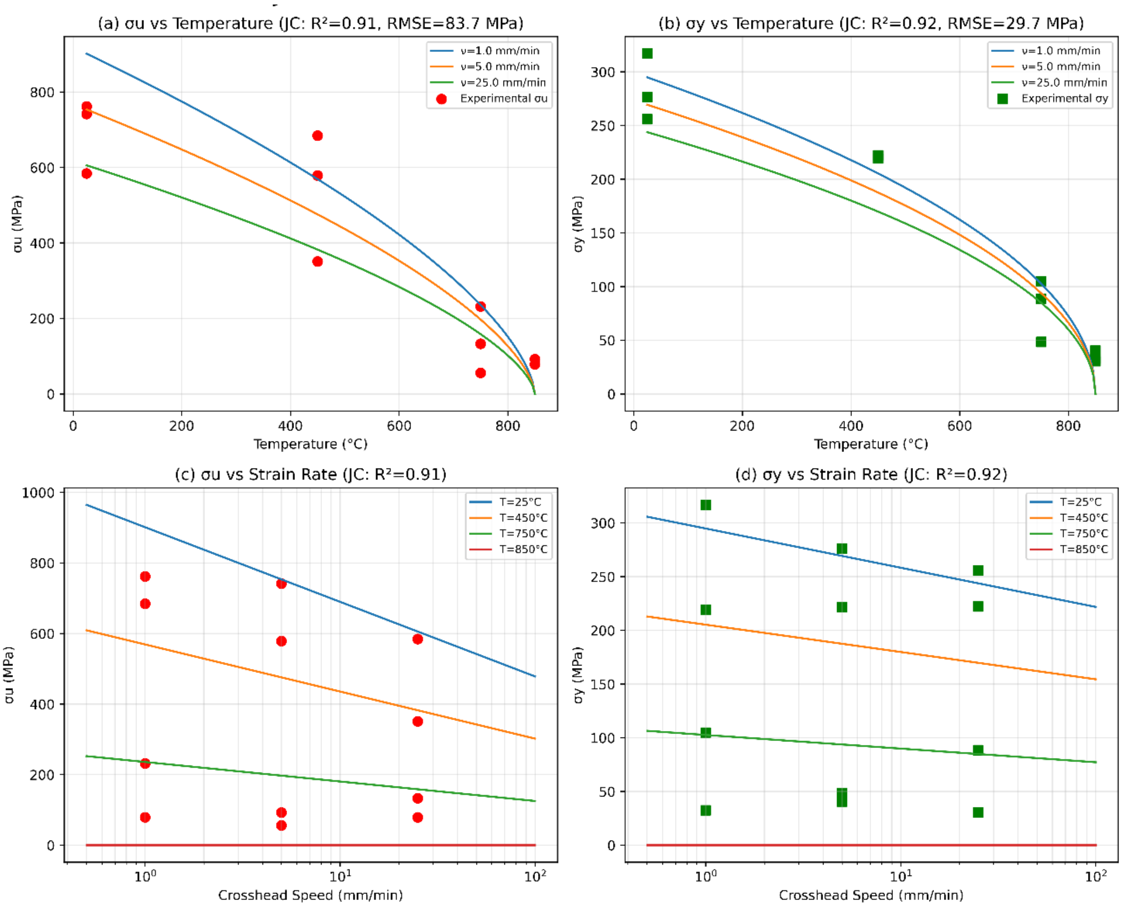

Fig. 9. Johnson-Cook approach for ductile cast iron: (a) σ_n vs. temperature, (b) σ_Y vs. temperature, (c) σ_n vs. strain rate, (d) σ_Y vs. strain rate

The strong agreement between the experimental results and model predictions demonstrates that the calibrated Johnson–Cook formulation provides a reliable representation of the thermo-mechanical response of the investigated ductile cast iron. Consequently, the validated constitutive equations were employed as the predictive framework for the subsequent multi-objective NSGA-II optimization procedure, enabling the simultaneous optimization of strength, ductility, and fracture toughness under elevated-temperature service conditions. While for yield strength modeling, the Johnson-Cook formulation is applied empirically, with fracture strain serving as an indirect proxy for the deformation state rather than a direct physical dependency. The small B value (23.98 MPa) relative to A (291.76 MPa) indicates that the strain hardening term contributes minimally, consistent with the fact that yielding occurs at low strains.

To evaluate the predictive reliability of the calibrated Johnson–Cook (JC) model, a residual analysis was conducted for ultimate tensile strength (σ_u) and yield strength (σ_Y), as shown in Figure 10.

Figure 10a indicates that the residuals for σ_u have a mean value of 14.8 MPa and a standard deviation of 82.4 MPa. Although several localized deviations are observed, the residuals are distributed around the zero-error baseline, indicating no systematic prediction bias.

For σ_Y (Figure 10b), the residuals exhibit a mean value of 17.4 MPa and a substantially lower standard deviation of 24.2 MPa, reflecting a more compact error distribution and improved predictive consistency.

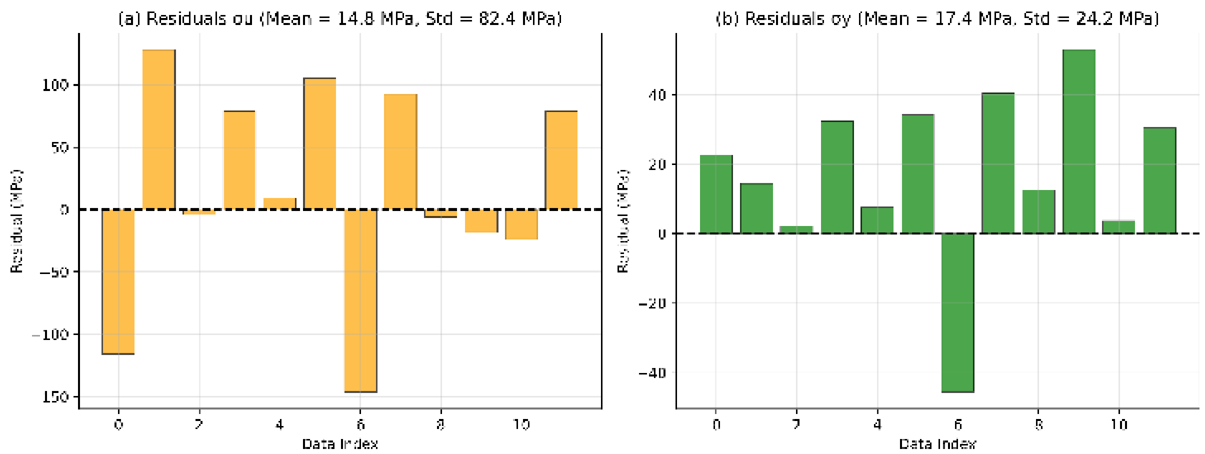

Fig. 10. Residuals of Johnson-Cook approach: (a) σ_n, (b) σ_Y, showing small deviations that highlight good predictive accuracy at varying temperatures and strain rates

Overall, the low mean residuals and balanced error distributions confirm the robustness of the calibrated Johnson–Cook model and support its use in the subsequent multi-objective NSGA-II optimization.

The Johnson-Cook model parameters were calibrated using a random search algorithm (N = 5000 iterations) to minimize the mean squared error (MSE) between predicted and experimental σu and σy values from Table 2. Random search was selected over gradient-based optimization methods (e.g., Levenberg-Marquardt) for the following reasons: (1) The MSE objective function for JC parameter calibration is non-convex and exhibits multiple local minima; gradient-based methods may converge to suboptimal local minima depending on initial guesses. (2) Random search provides a global exploration strategy across the entire parameter space without requiring derivatives or initial guesses. (3) With sufficient sampling (5000 iterations > 10× the 5-dimensional parameter space), random search provides a probabilistic approximation of the global optimum; with sufficiently large sampling, the probability of finding a near-optimal solution increases substantially. (4) This approach has been successfully applied in similar constitutive modeling studies for metallic materials [34, 40]. The parameter search bounds were: A ∈ [50, 1000], B ∈ [0, 1500], n ∈ [0.01, 0.8], C ∈ [-0.2, 0.8], m ∈ [0.1, 3.5]. The optimal parameters achieving minimum MSE are reported in Table 3.

4.4. Comparative Evaluation of Arrhenius and Johnson-Cook Constitutive Frameworks

To establish a robust constitutive description of the investigated ductile cast iron under elevated-temperature service conditions, a comparative assessment was conducted between the classical Arrhenius-type constitutive model and the phenomenological Johnson–Cook (JC) framework. The predictive capabilities of both models were evaluated using the coefficient of determination (R^2) and the root mean square error (RMSE).

For ultimate tensile strength (σ_u), the Arrhenius model yielded an R^2 value of 0.48 with an RMSE of 197.5 MPa, whereas the Johnson–Cook model achieved a substantially improved fit with R^2 = 0.91 and RMSE = 83.7 MPa. Similarly, for yield strength (σ_Y), the Arrhenius model produced R^2 = 0.51 and RMSE = 71.4 MPa, while the Johnson–Cook model attained R^2 = 0.92 and RMSE = 29.7 MPa.

The comparative analysis reveals a pronounced difference in the predictive performance of the two constitutive frameworks (see Tables 5 and 6). The Arrhenius formulation exhibits significant deviation from the experimental observations, as reflected by its relatively low R^2 values and high prediction errors. The model tends to oversimplify the thermo-mechanical response of the material by imposing rigid exponential and logarithmic relationships, resulting in nearly flat strain-rate trends and an over-constrained description of temperature-dependent softening. Consequently, it fails to accurately reproduce the nonlinear strength degradation observed within the intermediate temperature range of 450 °C to 750 °C.

DOI: 10.65731/ama/2026-0073

Tab. 6. Accuracy metrics for fracture strain and JIC regression models

Model	Target	R^2	RMSE
Linear regression (Eq. 5)	εf (%)	0.82	0.32%
Linear regression (Eq. 7)	JIC (kJ/m²)	0.89	5.8

In contrast, the Johnson–Cook formulation provides a markedly improved representation of the experimental behavior. The significant increase in R^2 values and reduction in RMSE demonstrate its superior capability to capture the coupled effects of strain-rate sensitivity and thermal softening. The multiplicative structure of the Johnson–Cook model enables the independent treatment of strain hardening, strain-rate effects, and temperature-dependent degradation, thereby offering sufficient flexibility to describe both yielding behavior and ultimate load-carrying capacity over the entire range of investigated testing conditions.

The comparatively poor performance of the Arrhenius model highlights the highly nonlinear nature of ductile cast iron under elevated-temperature conditions. Conversely, the strong agreement obtained using the Johnson–Cook framework validates its suitability as the constitutive model for the present study. Accordingly, the calibrated Johnson–Cook equations were adopted as the material model for the subsequent multi-objective NSGA-II optimization, providing a reliable predictive framework for the simultaneous optimization of strength, ductility, and fracture toughness.

These findings underscore the limited capability of the conventional Arrhenius formulation to replicate the experimental behavior of ductile cast iron across diverse thermomechanical conditions. The observed limitations are consistent with findings from comparative investigations involving other alloy systems. For example, in the context of hot compression testing of 316L stainless steel, both Arrhenius-type and Johnson–Cook models were found to be inadequate in accurately reproducing flow stress behavior across a wide range of temperatures and strain rates. In contrast, data-driven approaches, specifically artificial neural network models, demonstrated superior predictive performance, as confirmed by lower RMSE values and higher correlation coefficients [40]. Similarly, research on Ti_2AlNb-based intermetallic alloys revealed that Arrhenius-type formulations were only effective under low strain-rate conditions and within superplastic deformation regimes. In broader thermomechanical domains, modified Johnson–Cook models yielded more reliable predictions. These studies reinforce the conclusion that the classical Arrhenius law is insufficient for capturing the complex, multi-mechanistic behavior characteristic of ductile cast iron. This underscores the necessity of employing more advanced constitutive frameworks—such as physically motivated models or enhanced phenomenological formulations—to achieve robust and generalizable predictions under high-temperature and variable strain-rate conditions.

4.5. Non-dominated Sorting Genetic Algorithm II. (NSGA-II)

– **Fracture Toughness Interrelations (Pareto-Type Curves)**

Figure 11 illustrates the Pareto-optimal trade-offs obtained from the NSGA-II optimization, highlighting the relationships among fracture strain (ε_f), ultimate tensile strength (σ_u), and fracture toughness (J_{IC}). As shown in Figure 11a, fracture toughness decreases progressively with increasing fracture strain, indicating a trade-off between fracture resistance and ductility. Figure 11b demonstrates a positive correlation between ultimate tensile strength and fracture strain over much of the Pareto front, although the relationship becomes increasingly nonlinear at higher ductility levels. Similarly, Figure 11c reveals that higher ultimate tensile strengths are generally associated with increased fracture toughness, reflecting the coupled influence of thermo-mechanical processing conditions on both properties.

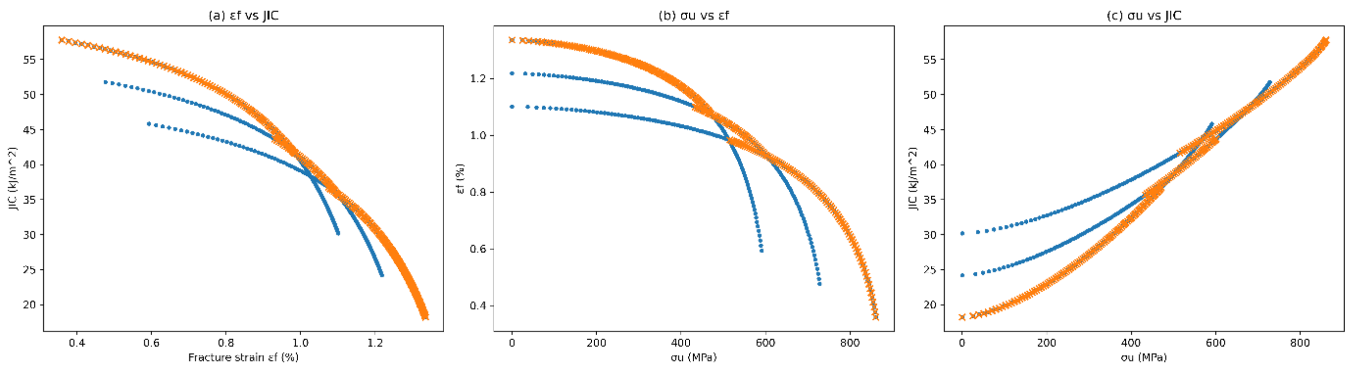

Fig. 11. Pareto fronts generated by NSGA-II optimization showing the relationships between (a) fracture strain (εf) and JIC, (b) ultimate tensile strength (σ_u) and fracture strain (εf), and (c) ultimate tensile strength (σ_u) and JIC

The close agreement between the experimental data and the Pareto-optimal solutions confirms the ability of the optimization framework to capture the underlying material behavior. The smooth Pareto fronts define the optimal balance among strength, ductility, and fracture resistance, demonstrating that improvements in one performance metric are often achieved at the expense of another. These results provide valuable insight into the competing mechanical responses of ductile cast iron and establish a quantitative basis for selecting processing conditions that satisfy specific engineering requirements.

Figure 12 shows the decision map which underscores the significance of Pareto optimization in the context of material design. The colored data points correspond to varying strain rates (i.e., crosshead speeds), while the red markers denote conditions that are Pareto-optimal. In contrast to single-objective optimization, Pareto analysis yields a spectrum of compromise solutions rather than identifying a singular optimal point. This enables engineers to navigate competing design objectives such as enhancing strength, ductility, and fracture toughness within a unified framework. Within the broader scope of multi-objective optimization, particularly when applied to data-driven modeling, Pareto fronts serve as a critical tool for informed decision-making under trade-off conditions. For example, increasing the strain rate may lead to improved ductility but diminished fracture toughness, whereas elevated temperatures might enhance toughness at the expense of strength. The Pareto front delineates the combinations of temperature and strain rate for which no single property can be improved without adversely affecting another. This form of visualization facilitates the identification of processing parameters that align with specific performance requirements such as prioritizing toughness for safety-critical applications or maximizing strength for structural components. This methodology parallels the use of multi-objective evolutionary algorithms (e.g., NSGA-II) in computational optimization. Rather than converging on a single solution, these algorithms generate a diverse set of Pareto-optimal outcomes. Practitioners can then select the most appropriate operating conditions based on contextual constraints and design priorities.

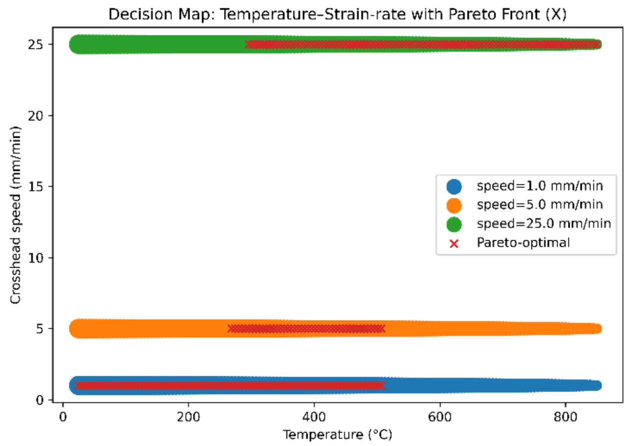

Fig. 12. Decision map of temperature–strain rate with Pareto-optimal front, illustrating optimal processing windows for ductile cast iron

From the NSGA-II Pareto front, four representative operating conditions are identified and listed in Table 7. The balanced condition (450°C, 5 mm/min) offers moderate strength (578.4 MPa), ductility (0.91%), and toughness (39.8 kJ/m²), representing a reasonable compromise for general engineering applications.

Tab. 7. Selected Pareto-optimal operating conditions from NSGA-II

Condition	T (°C)	Speed (mm/min)	σu (MPa)	εf (%)	JIC (kJ/m²)	Primary advantage
High strength	25	1	761.5	0.56	54.7	Max. strength
Balanced	450	5	578.4	0.91	39.8	Moderate all properties
High ductility	850	25	78.7	2.20	8.4	Max. elongation
High toughness	25	5	741.3	0.54	52.9	Max. JIC

The comparison between the grid-based Pareto set and the NSGA-II-generated Pareto front (Figure 13) demonstrates the effectiveness of evolutionary optimization in exploring the thermo-mechanical design space of ductile cast iron. The grid-based Pareto solutions, derived from the experimentally evaluated temperature and strain-rate combinations, define the primary trade-off between fracture strain (εf) and fracture toughness (J_{IC}). These solutions establish a discrete Pareto boundary representing the best experimentally observed combinations of competing mechanical properties.

The NSGA-II Pareto front closely follows the trend of the grid-based solutions while providing a denser and more continuous representation of the Pareto-optimal region. By exploring a continuous decision space, NSGA-II identifies additional feasible solutions between the experimentally sampled conditions and extends the Pareto front toward both higher fracture toughness and higher fracture-strain regimes. This capability enables a more comprehensive characterization of the trade-off between ductility and fracture resistance.

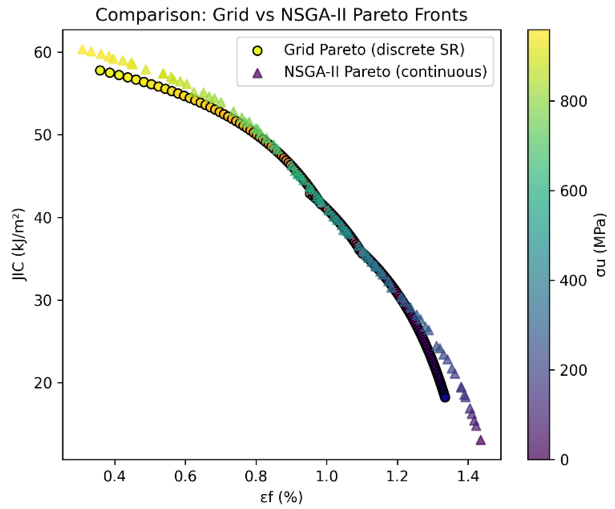

Fig. 13. Comparison of grid-based Pareto front (discrete strain rates) and NSGA-II Pareto front (continuous search space), showing the expansion of optimal solutions for ductile cast iron processing

The strong overlap between the two Pareto fronts confirms the consistency of the optimization framework and indicates that the experimentally derived solutions are located near the true Pareto-optimal boundary. At the same time, the NSGA-II results broaden the design space by revealing additional processing conditions that were not directly investigated experimentally but are predicted to provide competitive performance.

Overall, the combined analysis validates the experimental observations while demonstrating the value of NSGA-II as a tool for identifying optimal thermo-mechanical processing conditions. The results highlight its potential for accelerating material design and supporting decision-making in applications requiring a balance between fracture toughness and ductility (e.g., Juncaili et al. [60]; Zhou et al. [61]).

4.6. Limitation

No experimental validation exists for the XFEM predictions at elevated temperatures (450°C, 750°C, 850°C) or for higher strain rates (SR2 and SR3). The only available experimental validation was performed at room temperature (25°C) for SR1 condition (1.8×10^{-4} s^{-1}) against the compact tension test results of Kobayashi and Yamada [19], which confirmed the model's reliability with

DOI: 10.65731/ama/2026-0073

an error of less than 6.3%. Based on this validation, the XFEM model was deemed acceptable for predicting J_{IC} values under other conditions. The model was therefore extended to elevated temperatures and higher strain rates by systematically updating only the mechanical properties (Young's modulus, ultimate strength, yield strength, and fracture strain) at each temperature and strain rate condition, as reported in Table 2. The finite element model originally presented in the main reference [47] has been completely rebuilt and re-evaluated using these mechanical properties. All J_{IC} values presented in Table 4 (SR1, SR2, and SR3) were extracted from this re-evaluated XFEM model. While this approach is scientifically sound given the validated model, the lack of direct experimental confirmation at elevated temperatures and higher strain rates remains a limitation of the present study. Future work should include experimental J_{IC} measurements under these conditions to further validate the predictions.

5. CONCLUSIONS

This study provides a comprehensive experimental, numerical, and optimization-based assessment of the thermo-mechanical behavior of ductile cast iron over a wide range of temperatures and strain rates. The results demonstrate that the mechanical response of the material is strongly governed by the coupled effects of thermal softening and strain-rate sensitivity. Both ultimate tensile strength (σ_u) and yield strength (σ_Y) decreased progressively with increasing temperature, while ductility increased substantially. Young's modulus declined with increasing temperature for all strain rates. For SR1 (1.8×10^{-4} s^{-1}), it decreased from 240 GPa at 25°C to 105 GPa at 850°C, while for SR3 (4.5×10^{-3} s^{-1}), it declined from 171 GPa at 25°C to 37 GPa at 850°C. The fracture strain (εf) reached a maximum value of 2.20% at 850 °C, indicating a transition toward enhanced plastic deformation at elevated temperatures. XFEM-based fracture simulations further revealed a pronounced reduction in fracture toughness (J_{IC}), decreasing from 54.66 kJ/m² at room temperature to 23.9 kJ/m² at 850 °C, highlighting the progressive deterioration of crack-growth resistance under severe thermal exposure.

A comparative evaluation of constitutive frameworks demonstrated the limitations of the classical Arrhenius formulation in describing the highly nonlinear thermo-mechanical behavior of ductile cast iron. The Arrhenius model exhibited poor predictive capability, with coefficients of determination of only 0.48 and 0.51 for σ_u and σ_Y, respectively. In contrast, the Johnson–Cook (JC) formulation accurately reproduced the experimental trends, achieving R^2 values of 0.91 for σ_u and 0.92 for σ_Y while significantly reducing prediction errors. Residual analysis confirmed the statistical robustness of the calibrated model and the absence of systematic prediction bias. These findings establish the Johnson–Cook framework as a reliable constitutive representation for ductile cast iron subjected to elevated-temperature loading conditions.

Beyond constitutive characterization, the integration of the calibrated JC model with NSGA-II multi-objective optimization enabled a quantitative exploration of the competing relationships among strength, ductility, and fracture toughness. The resulting Pareto fronts identified optimal processing windows spanning high-strength, high-ductility, balanced-performance, and high-toughness regimes, thereby providing a practical decision-making framework for component design and process selection. The close agreement between experimentally derived Pareto solutions and the continuous NSGA-II frontier further validates the predictive capability of the proposed optimization strategy.

The principal contribution of this work lies in establishing a unified experimental–computational framework that combines thermo-mechanical testing, fracture simulation, constitutive modeling, and evolutionary multi-objective optimization. This integrated methodology not only improves the understanding of the degradation mechanisms governing ductile cast iron at elevated temperatures but also provides a transferable framework for the design and optimization of engineering alloys operating under complex thermo-mechanical environments.

Nevertheless, the current optimization was restricted to temperature and strain rate as decision variables, reflecting the available experimental design. Future studies should incorporate additional metallurgical variables, including alloy chemistry, graphite morphology, and heat-treatment parameters, to further expand the design space. Moreover, targeted experimental validation of the NSGA-II-predicted Pareto-optimal conditions will be essential for confirming the model predictions at previously unexplored thermo-mechanical regimes and for advancing the development of data-driven materials design methodologies.

REFERENCES

1. Trelles EG, Eckmann S, Schweizer C. Experimental characterization of the short crack growth behavior of a ductile cast iron (DCI GJS-500) affected by intergranular embrittlement at temperatures nearby 400 °C. Int J Fatigue. 2022;155:106573.
2. Fonte M, Infante V, Freitas M, Reis L. Failure mode analysis of two diesel engine crankshafts. Procedia Struct Integr. 2016;1:313-8.
3. Sertucha J, Suárez R, Izaga J, Hurtado L, Legazpi J. Prediction of solid state structure based on eutectic and eutectoid transformation parameters in spheroidal graphite irons. Int J Cast Met Res. 2006;19:315-22.
4. Asi O. Failure of a diesel engine injector nozzle by cavitation damage. Eng Fail Anal. 2006;13:1126-33.
5. Hou XQ, Li Y, Jiang T. Fracture failure analysis of ductile cast iron crankshaft in a vehicle engine. J Fail Anal Prev. 2011;11:10-6.
6. Moore D, Packer K, Jones A, Carlson D. Crankshaft failure and why it may happen again. Pract Fail Anal. 2001;1:63-72.
7. Mottitschka T, Pusch G, Biermann H, Zybell L, Kuna M. Influence of graphite spherical size on fatigue behaviour and fracture toughness of ductile cast iron EN-GJS-400-18LT. Int J Mater Res. 2012;103:87-96.
8. de La Torre U, Lacaze J, Sertucha J. Chunky graphite formation in ductile cast irons: effect of silicon, carbon and rare earths. Int J Mater Res. 2016;107:1041-50.
9. Kasvayee KA. Microstructure and deformation behaviour of ductile iron under tensile loading [dissertation]. Jönköping: Jönköping University, School of Engineering; 2015.
10. Dong M, Prioul C, François D. Damage effect on the fracture toughness of nodular cast iron: Part I. Damage characterization and plastic flow stress modeling. Metall Mater Trans A. 1997;28:2245-54.
11. Xiang S, Jonsson S, Babu RP, Zhu B, Odqvist J. Influence of tension and compression dwell on the creep-fatigue properties of the austenitic cast iron Ni-resist D5S. Mater Sci Eng A. 2021;814:141179.
12. Öberg C, Zhu B, Jonsson S. Creep behaviour, creep damage and precipitation in the austenitic ductile cast iron D5S at 750 °C. Mater Sci Eng A. 2021;802:140662.
13. Öberg C. Creep Behavior of High Temperature Cast Materials for Exhaust Applications [dissertation]. Stockholm: KTH Royal Institute of Technology; 2020.
14. de la Torre U, González-Martínez R, Méndez S. Effect of the section size, holding temperature and time on the kinetics of the ausferritic transformation and mechanical properties of as-cast ausferritic ductile iron. Mater Sci Eng A. 2020;788:139536.
15. Angella G, Taloni M, Donnini R, Zanardi F. The Correlation between

Solidification Rates, Microstructure Integrity and Tensile Plastic Behaviour in 4.2 wt.% Silicon Strengthened Ductile Iron. J Cast Mater Eng. 2022;6:1-8.

16. Pacha-Gołębiowska H, Piekarska W. Mechanical properties of ductile cast iron relation to the charge elements. In: IOP Conference Series: Materials Science and Engineering. 2021. p. 012022.
17. Wu X, Quan G, MacNeil R, Zhang Z, Sloss C. Failure mechanisms and damage model of ductile cast iron under low-cycle fatigue conditions. Metall Mater Trans A. 2014;45:5085-97.
18. Bendikiene R, Ciuplys A, Cesnavicius R, Jutas A, Bahdanovich A, Marmysh D, et al. Influence of austempering temperatures on the microstructure and mechanical properties of austempered ductile cast iron. Metals. 2021;11:967.
19. Kobayashi T, Yamada S. Evaluation of static and dynamic fracture toughness in ductile cast iron. Metall Mater Trans A. 1994;25:2427-36.
20. Artola G, Monzón A, Lacaze J, Sertucha J. Tensile properties and fracture toughness at service temperatures of an optimized pearlitic ductile iron alloy for automotive crankshafts. Mater Sci Eng A. 2022;831:142206.
21. Boulifa I, Hadji A. Study of the influence of alloying elements on the mechanical characteristics and wear behavior of a ductile cast iron. Frattura ed Integr Strutt. 2021;15:74-83.
22. Eric O, Sidjanin L, Miskovic Z, Zec S, Jovanovic M. Microstructure and toughness of CuNiMo austempered ductile iron. Mater Lett. 2004;58:2707-11.
23. Putatunda SK. Influence of austempering temperature on fracture toughness of a low manganese Austempered Ductile Iron (ADI). Mater Manuf Process. 2001;16:245-63.
24. Putatunda SK. Development of austempered ductile cast iron (ADI) with simultaneous high yield strength and fracture toughness by a novel two-step austempering process. Mater Sci Eng A. 2001;315:70-80.
25. Berdin C, Haušild P. Damage Mechanisms and Local Approach to Fracture: Part I: Ductile fracture. Transf Fract Mech Charact. 2002:167-80.
26. Berdin C, Dong M, Prioul C. Local approach of damage and fracture toughness for nodular cast iron. Eng Fract Mech. 2001;68:1107-17.
27. Jing Z. Prediction of failure of cast iron with dynamic loading and high temperature. Mater Sci Eng A. 2013;566:71-81.
28. Joshi A, Baxevanakis KP, Silberschmidt VV. High-temperature creep of cast irons. In: Solid Mechanics, Theory of Elasticity and Creep. Springer; 2023. p. 147-73.
29. Basurto-Hurtado JA, Perez-Soto G, Osornio-Rios RA, Dominguez-Gonzalez A, Morales-Hernandez L. A new approach to modeling the ductile cast iron microstructure for a finite element analysis. Arab J Sci Eng. 2019;44:1221-31.
30. Mirzadeh H, Cabrera JM, Najafizadeh A. Modeling and Prediction of Hot Deformation Flow Curves. Metall Mater Trans A. 2012;43:108-23.
31. Bodunrin MO. Flow stress prediction using hyperbolic-sine Arrhenius constants optimised by simple generalised reduced gradient refinement. J Mater Res Technol. 2020;9:2376-86.
32. Farabi E, Zarei-Hanzaki A, Abedi HR. High Temperature Formability Prediction of Dual Phase Brass Using Phenomenological and Physical Constitutive Models. J Mater Eng Perform. 2015;24:209-20.
33. Johnson GR. A constitutive model and data for metals subjected to large strains, high strain rates and high temperatures. In: Proceedings of the 7th International Symposium on Ballistics. Am. Def. Prep. Org. (ADPA), Netherlands; 1983:541-7.
34. Abbasi-Bani A, Zarei-Hanzaki A, Pishbin MH, Haghdadi N. A comparative study on the capability of Johnson–Cook and Arrhenius-type constitutive equations to describe the flow behavior of Mg–6Al–1Zn alloy. Mech Mater. 2014;71:52-61.
35. Xie Z, Guan Y, Lin J, Zhai J, Zhu L. Constitutive model of 6063 aluminum alloy under the ultrasonic vibration upsetting based on Johnson-Cook model. Ultrasonics. 2019;96:1-9.
36. Raut N, Shinde S, Yakkundi V. Determination of Johnson Cook parameters for Ti-6Al-4V Grade 5 experimentally by using three different methods. Mater Today Proc. 2021;44:1653-8.
37. Razali MK, Irani M, Joun M. General modeling of flow stress curves of alloys at elevated temperatures using bi-linearly interpolated or closed-form functions for material parameters. J Mater Res Technol. 2019;8:2710-20.
38. Sellars C, McTegart WJ. On the mechanism of hot deformation. Acta Metall. 1966;14:1136-8.
39. Ashtiani HRR, Shahsavari P. A comparative study on the phenomenological and artificial neural network models to predict hot deformation behavior of AlCuMgPb alloy. J Alloys Compd. 2016;687:263-73.
40. Esmaeilpour A, Abedi HR. Comparing the Capability of Phenomenological (Johnson-Cook and Arrhenius-Type) and Artificial Neural Network Models in Predicting the Hot Deformation Behavior of Additively Manufactured 316L Stainless Steel. Iran J Mater Form. 2022;9:62-73.
41. Sinha A, Sikdar S, Chattopadhyay PP, Datta S. Optimization of mechanical property and shape recovery behavior of Ti-(~49at.%) Ni alloy using artificial neural network and genetic algorithm. Mater Des. 2013;46:227-34.
42. Gou W, Shi ZZ, Zhu Y, Gu XF, Dai FZ, Gao XY, et al. Multi-objective optimization of three mechanical properties of Mg alloys through machine learning. Mater Genome Eng Adv. 2024;2:e54.
43. Chen J, Yang T, Chen S, Jiang Q, Li Y, Chen X, et al. Multi-Objective Process Parameter Optimization of Ultrasonic Rolling Combining Machine Learning and Non-Dominated Sorting Genetic Algorithm-II. Materials. 2024;17.
44. Lin Y, Ma J, Lai D, Zhang J, Li W, Li S, et al. Multi-response optimization of process parameters in nitrogen-containing gray cast iron milling process based on application of non-dominated ranking genetic algorithm. Heliyon. 2022;8:e11629.
45. Gunpinar E, Khan S. A multi-criteria based selection method using non-dominated sorting for genetic algorithm based design. Optim Eng. 2020;21:1319-57.
46. Yang SH, Natarajan U. Multi-objective optimization of cutting parameters in turning process using differential evolution and non-dominated sorting genetic algorithm-II approaches. Int J Adv Manuf Technol. 2010;49:773-84.
47. Abdellah MY, Alharthi H, Alfattani R, Suker DK, Abu El-Ainin H, Mohamed AF, et al. Mechanical properties and fracture toughness prediction of ductile cast iron under thermomechanical treatment. Metals. 2024;14:352.
48. Abdellah MY, Hassan MK, El-Ainin HA. Plasticity and formability controlling of cast iron using thermo-mechanical treatment. Am J Mater Eng Technol. 2014;2:38-42.
49. ASTM E8. Standard test methods for tension testing of metallic materials. Annual Book of ASTM Standards. ASTM International; 2001.
50. Deb K, Pratap A, Agarwal S, Meyarivan T. A fast and elitist multiobjective genetic algorithm: NSGA-II. IEEE Trans Evol Comput. 2002;6:182-97.
51. Montgomery DC, Peck EA, Vining GG. Introduction to linear regression analysis. John Wiley & Sons; 2021.
52. Nishi S. Fragilisation par revenu de la fonte a graphite spheroidal [dissertation]. Lille: Université de Lille; 1976.
53. Kobayashi T. Ductile cast iron. In: Strength and toughness of materials. Springer; 2004. p. 89-110.
54. Den Uijl N, Carless L. Advanced metal-forming technologies for automotive applications. In: Advanced materials in automotive engineering. Elsevier; 2012. p. 28-56.
55. Levy B, Van Tyne C. Effect of a strain-hardening rate at uniform elongation on sheared edge stretching. J Mater Eng Perform. 2012;21:2147-54.
56. Konovalenko I, Maruschak P, Prentkovskis O. Automated method for fractographic analysis of shape and size of dimples on fracture surface of high-strength titanium alloys. Metals. 2018;8:161.
57. Haitao X, Dengke W, Kaihong S. Effect of deformation temperature on mechanical properties and microstructure of TWIP steel for expansion tube. High Temp Mater Process. 2020;39:63-73.
58. Chaudry UM, Jaafreh R, Malik A, Jun TS, Hamad K, Abuhmed T. A Comparative Study of Strain Rate Constitutive and Machine Learning Models for Flow Behavior of AZ31-0.5 Ca Mg Alloy during Hot Deformation. Mathematics. 2022;10:766.
59. Liu C, Sun D, Zhang X, Andrieux F, Gersterc T. Extension of Flow

Behaviour and Damage Models for Cast Iron Alloys with Strain Rate Effect. Chin J Mech Eng. 2024;37:61.
60. Li J, Yang Y, Chen L, Yu T, Zhao J, Wang Z. Multi-Objective Optimization of Process Parameters in Laser DED Ni-Based Powder on Steel Rail Using Response Surface Design. Coatings. 2024;14:401.
61. Zhou Y, Wang Z, Tao W, Sun Y, Wu J, Wang G, et al. Multi-objective optimization design of Al-Si alloys based on machine learning. Calphad. 2025;90:102870.

The authors would also like to express their sincere gratitude to Prof. Dr. Hamed Abo-El-Aanin, Eng. Ahmed Ezzat, and Eng. Rania Gomaa for their valuable assistance in conducting the experimental work associated with this study.

Mohammed Y. Abdellah: https://orcid.org/0000-0003-2538-3207

Shadi Salem: https://orcid.org/0000-0001-6702-0282

Hasan H. Hijji: https://orcid.org/0000-0001-9977-3000

Ahmed Mallouli: https://orcid.org/0000-0001-7538-1774